

Concurrent Precipitation of Nb(C,N) and Metastable $M_{23}C_6$ in Alloy 347H at 700°C and 750°C: Computer Simulations and Comparison to Experiment

Michael V. Glazoff^(1,*), Michael C. Gao⁽²⁾, Laurent Capolungo⁽³⁾, Michael P. Brady⁽⁴⁾, Gabriel O. Ilievbare⁽¹⁾, Yukinori Yamamoto⁽⁴⁾, Qing-Qiang Ren⁽⁴⁾, Jonathan D. Poplawsky⁽⁴⁾, Jianguo Yu⁽¹⁾, and Feng Zhang⁽⁵⁾

⁽¹⁾Idaho National Laboratory; ⁽²⁾National Energy Technology Laboratory; ⁽³⁾Los Alamos National Laboratory; ⁽⁴⁾Oak Ridge National Laboratory; ⁽⁵⁾Ames Laboratory

Abstract We present our results for the concurrent precipitation of the metastable $M_{23}C_6$, the Nb(C,N) secondary precipitates, and the Nb(C,N) primary crystals in 347H austenitic stainless steel (XMAT Program). For precipitation modeling, we accounted for the elastic contribution to interfacial energy and for the Fe-spin-polarization for NbC/Fe and $M_{23}C_6$ /Fe interfacial energy values. With these corrections, a value of the DFT-calculated NbC/Fe interfacial energy increased to ~ 0.63 J/m². For $M_{23}C_6$ precipitates, an error function was used to describe the interfacial energy growth with particle size. In precipitation simulations, the average size of the *primary* Nb(C,N) particles remained ~ 1 μ m at 700°C and ~ 0.3 μ m at 750°C. $M_{23}C_6$ precipitates at 750°C dissolved after 120 hours (experiment-300 hours). The Nb(C,N)/Fe interfacial energy was not affected by the nitrogen additions. With these modifications, reasonable agreement with the available experimental data was obtained, which allows using them in the development of the 2nd-phase particle informed creep theory.

Introduction

A significant interest of the materials community is drawn today to the quantitative modeling of concurrent precipitation in heterogeneous materials [1-6]. Understanding and controlling concurrent precipitation in heterogeneous materials is of primary importance for the properties of materials. Indeed, the ability to describe precipitation and microstructure evolution (mean-field approximation) leads to the design of optimized heat treatments of structural alloys, continuous cooling transformation (CCT) and time temperature transformation (TTT) diagrams, and to microstructure-based modeling of the mechanical behavior of materials. In turn, this capability development is part of a broad trend toward understanding the “materials genome” and using a systems approach called integrated computational materials engineering (ICME) for computationally-intensive design of novel materials and “digital twins” [7-12]. The theoretical framework developed some 50 years ago and even earlier [13-17] was implemented in several codes. In all precipitation modeling and simulation efforts reported here, the TC-PRISMA software was used [18]. It implements a physics-based approach based upon the Langer-Schwartz theory and its development and numerical implementation in the Kampmann-Wagner (Numerical) approach [13-15]. It was developed to solve a set of coupled mass balance and continuity integral-differential equations written out for the particle size distribution function evolution with particle size and time. To achieve that goal, one needs to use physics-based approximations for (A): the particle nucleation rate, and (B): the particle growth rate. All the discussion that follows is based upon the TC-PRISMA software manuals [18].

Nucleation For the nucleation rate, the “Classical Nucleation Theory is used (the Zel’dovich-Frenkel equation) [16,17]. In this approach, the particle nucleation rate $J(t)$ needs to be expressed as a function of time, the steady state nucleation rate J_s ; and the incubation time, τ , see Eqn. 1:

$$J(t) = J_s \exp(-\tau/t) \quad (1)$$

The steady state nucleation rate J_s depends upon the Zel’dovich factor Z , the molecular attachment rate β^* , the number of potential nucleation sites N that depend upon the character of nucleation (homogeneous vs heterogeneous), and the barrier for nucleation, ΔG^* , Eqn. 2:

$$J_s = Z\beta^* N \exp(-\Delta G^*/kT) \quad (2)$$

For the incubation time τ , and the molecular attachment rate β^* we have the following equations:

$$\tau = \frac{1}{4\pi Z^2 \beta^*} \quad (3)$$

$$\beta^* = \frac{4\pi(r^*)^2}{a^4} \left\{ \sum_{i=1}^k \frac{(X_i^{\beta/\alpha} - X_i^{\alpha/\beta})^2}{X_i^{\beta/\alpha} D_i} \right\}^{-1} \quad (4)$$

The critical radius r^* is expressed as [Type equation here](#).

$$r^* = \frac{2\sigma V_m}{\Delta G_m} \quad (5)$$

ΔG^* is expressed as a function of σ (precipitate/matrix interfacial energy); V_m (molar volume of precipitate); and ΔG_m (the driving force of nucleation), Eqn.6:

$$\Delta G^* = (16\pi\sigma^3 V_m^2) / (3\Delta G_m^2) \quad (6)$$

In equation (5) and (6), σ is the interfacial energy for the precipitate/matrix interface, ΔG_m is the driving force of precipitation, and a is the lattice parameter. The values $X_i^{\beta/\alpha}$ and $X_i^{\alpha/\beta}$ stand for the molar fraction of component “ i ” at the interface for the precipitate and the matrix, respectively [18-22].

The overall number of parameters and variables entering equations (1-6) makes the “head-on” approach to solving the original mass balance and continuity equations impossible without approximations. In computational practice, it is important that such parameters as the nucleation driving force ΔG_m , the molar volume of precipitate V_m , and the diffusivity D_i of the i^{th} component in the matrix, *can all be obtained from the corresponding thermodynamic and mobility databases*.

This is why TC-PRISMA requires that both types of databases be used in precipitation calculations.

Particle Growth Rate This term also requires making approximations and assumptions to describe precipitation in different types of alloys. Among the existing models, one should mention the binary model by Aaron et al. [23], the multi-component coarsening model by Morral and Purdy [24], the model developed and implemented in the *PrecipiCalc* software by Jou, Voorhees and Olson (Questek, LLC) [25]; the model proposed by Guo and Sha [26], the “similarity-supersaturation” model by Sourmail [27,28]; and the “thermodynamic extremum principle” model by Svoboda et al. [29].

In a recent publication [30], the nucleation kinetics in a multicomponent supersaturated solid solution was revisited using a combination of a thermodynamic extremum principle and the Fokker-Planck equation. The proposed general formalism included two limiting cases: bulk diffusion control, and the interfacial mobility control of nucleation kinetics. The growth law for multicomponent alloys was derived in the general case, when both mechanisms were considered [30].

In TC-PRISMA, a unique set of growth models was developed that follows the principle of local equilibrium and the flux balance equation. Its integration was performed using the moving interface approach implemented in the DICTRA software for diffusion modeling and simulation in multicomponent “heterogeneous” systems [31]. TC-PRISMA offers three growth models of the different degree of complexity:

(A): the pseudo-steady state growth model that accounts for low supersaturations and only diagonal terms of the mobility matrix (called “*Simplified*”);

(B): the pseudo-steady state plus cross-diffusion based upon the work of Morral and Purdy (called “*General*”) [24]. It also works for low supersaturations but should be used in those cases when a system contains a substitutional element with high melting temperature and low diffusivity. (C): Analytical Flux Balance Approximation (called “*Advanced*”). This model should be used when a system contains an interstitial element with very high diffusivity [22]. The last model is the most computationally expensive but allows to account for the high degrees of supersaturation and the cross-diffusion terms [22]

Concurrent Precipitation Simulation in 347H.

For the 347H austenitic stainless steel we used the standard (simplified) models for nucleation and growth described above. We had to perform additional DFT research (*Ibid.*, see Yu et al. [28]) to re-evaluate the NbC/fcc-Fe interface for the secondary NbC, Nb(C,N), and Nb(C,N,B) precipitates. For the metastable $M_{23}C_6$ phase that appeared before the stable NbX and the SIGMA phases¹, we needed to develop an analytic expression that took into consideration the variation of the interfacial energy with time and particle growing size. For the 700°C and 750°C calculations, the temperature dependence of the interfacial energy was insignificant. Finally, at 750°C, working with the Simplified Model, we were not able to reproduce the whole cascade of transformations “Primary NbC - Metastable $M_{23}C_6$ + stable NbX - SIGMA phase. The difficulty was in the extremely low driving force for the SIGMA phase and the numerical breakdown of the integration algorithms.

¹ Metastable phase usually nucleate and grow before any stable phases, mainly for two reasons: higher driving force of their formation, and lower mismatch between crystalline lattices (M₂₃C₆/fcc-Fe)

All other parameters were set at default values recommended in TC-PRISMA [18]. Following [1-5], we tried to develop the precipitation model with the least number of user-defined inputs. We varied only the total number of nucleation sites (type of precipitation), interfacial energies (see above), dislocation densities (to mimic the dislocation density growth with progression of creep). To add the 4th phase (SIGMA) to the cascade of concurrent precipitation we will vary the free energy addition factor (to change the driving force) and the mobility enhancement factor.

1.1 Concurrent precipitation of secondary NbC and metastable M₂₃C₆ from heat-treated alloy 347H

To obtain the optimal interfacial energy values for both precipitates, DFT calculations were performed [32]. These new results provided guidance for the Nb(C,N) precipitate: when accounting for the spin polarization of Fe atoms, the interfacial energy was higher than the default value of 0.32 J/m² (eventually the value of 0.63 J/m² was used). For the fast growing M₂₃C₆ precipitates it was established that the correct description of its precipitation kinetics must account for the variation of the interfacial energy with the growing precipitate size, at least up to the average size of 30 nm (and saturating at the thermodynamic limit of the flat surface). The error function and the logistic functions yielded the best results, and the following expression was developed (“*r*” stands for radius of a growing particle):

$$\sigma(\text{Fe}/\text{M}_{23}\text{C}_6) = (0.002 + 0.125) + 0.125 \cdot \text{erf}((r - 2.7 \cdot 10^{-10})/10^{-10}) \quad [\text{J}/\text{m}^2] \quad (7)$$

This expression for the fcc-Fe/M₂₃C₆ interfacial energy were identified after a significant number of trials (more than a hundred simulation runs on TC-PRISMA), which in some cases took as much as 15 minutes of the CPU time on a Dell Latitude 7490 laptop with 32 Gb of RAM and Intel i7 quadcore processor of the 8th generation. This is the reason why AI/ML approach will be employed that will yield reduced order models (ROMs) allowing to provide quick results and answering different “what-if” questions. This work is planned for the fiscal year 2022.

The considerations described above were tested against the TEM and SEM quantitative experimental results found in the literature for both secondary Nb(C,N) and metastable M₂₃C₆ precipitates [33,34]. The 347H alloy composition studied in [33,34] is given in Table 1:

Table 1. Chemical composition of the investigated type 347H austenitic steel wt% as given in [33,34]

Chemical Element	C	Cr	Ni	Nb	N	Mn	P	Mo	S	Fe
Composition, wt.%	0.059	17.60	10.71	0.54	0.013	1.59	0.024	0.116	0.0008	Bal.

In our simulations only P and S were omitted. The simulation results in Fig. 1 correspond to the experimental data obtained in [29]. For the average Nb(C,N) particle size after 2,200 hours of annealing at 700°C, the value of ~86 nm was reported [33] (~150nm in our simulations). Data on the particle size distribution and volume fraction of the metastable M₂₃C₆ precipitate were absent in that paper.

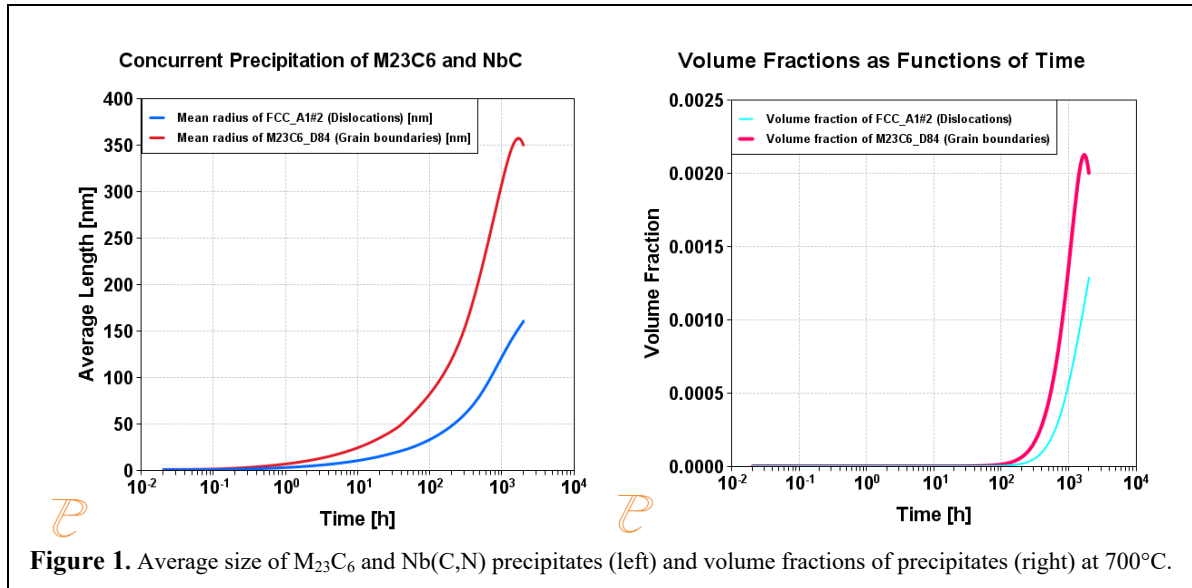


Figure 1. Average size of $M_{23}C_6$ and Nb(C,N) precipitates (left) and volume fractions of precipitates (right) at 700°C.

We found some additional results on the $M_{23}C_6$ and Nb(C,N) particle size evolution in [34]. These results included both the SEM and TEM experimental work. At 700°C, the average $M_{23}C_6$ particle size was $\sim 1\mu\text{m}$ after 2,200 hours of isothermal annealing [34]. Quantitative TEM data were reported only for annealing for 100 hours at different temperatures (700°C; 800°C; 850°C; and 900°C). The average Nb(C,N) particle size was consistent with the results reported in [29,30] and with our simulation results ($\sim 35\text{ nm}$ – simulation; 46 nm – experiment in [33,34]).

We conclude that a reasonable agreement between our simulations and experimental results [33,34] was achieved. More work is necessary to achieve even better agreement if such work is deemed necessary.

1.2 Modeling concurrent precipitation of primary Nb(C,N), secondary Nb(C,N), and metastable $M_{23}C_6$ precipitates

To obtain good results with TC-PRISMA the alloy composition used in simulations must closely follow the sequence of the heat treatment operations that it had been subjected to. Since the 347H alloy considered in [33,34] was subjected to normalizing (solutionizing) heat treatment at 1150°C for 0.5 hours, the primary Nb(C,N) particles forming directly upon solidification needed to be eliminated from consideration to model the concurrent precipitation of the secondary Nb(C,N) and metastable $M_{23}C_6$. Therefore, a correction for those primary Nb(C,N) particles was made in the concentrations of C, Nb, and Nb available for the secondary precipitation at working temperatures (700°C and 750°C).

However, there is a more elegant way to include into consideration primary, secondary Nb(C,N) and $M_{23}C_6$ in a single simulation run. Then, we use *the full alloy composition* (Table 1) for all simulation runs and a TC-PRISMA advanced option “Use Pre-existing Distribution”. Equilibrium Thermo-Calc calculations allow to calculate the volume fraction of the primary NbC particles (i.e., forming directly upon solidification) and the concentration of carbon in them. After that, the average particle size must be determined experimentally or hypothesized. In [33,34] the average size of the primary NbC particles was determined as $\sim 1\mu\text{m}$. Using these results, we constructed the size distribution of the primary NbC particles and used it in all

subsequent TC-PRISMA runs. The advantage of this approach is that we can monitor the particle size evolution for all three types of particles, on one graph, see Figure 2.

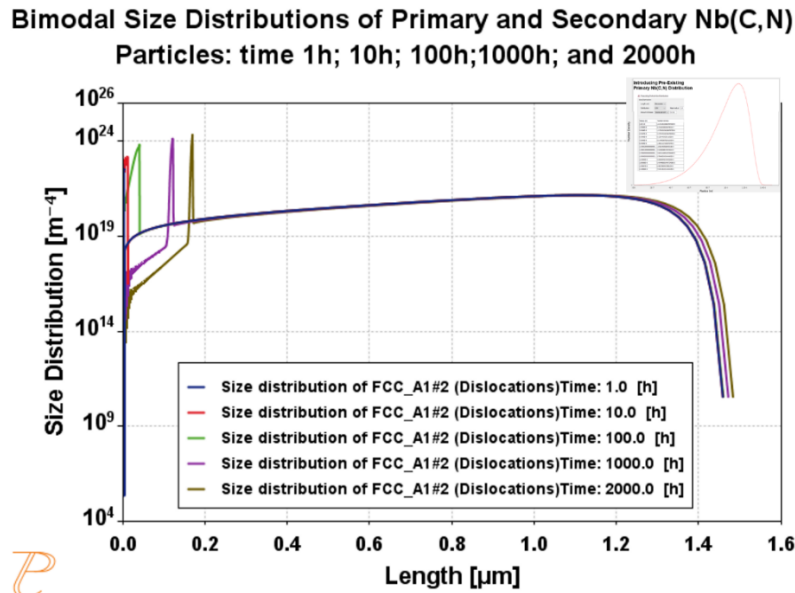


Figure 2. Size distributions of the primary and secondary NbC particles at different times: 1; 10; 100; 1000; and 2000 hours. The secondary precipitates are characterized by a smaller size; the primary NbC have the average particles size of $\sim 1\mu\text{m}$. Inlet (top right) illustrated the generated distribution of the primary Nb(C,N) particles used in simulation

These results are important because the primary NbC particles are practically not changing their size, while the secondary display growth. Both trends are consistent with the results reported in [33,34]

2.3 Precipitation of Secondary NbC and Metastable $M_{23}C_6$ at 750°C: XMAT Data and TC-PRISMA Simulations

On the property equilibrium diagram (phase composition as a function of temperature), the $M_{23}C_6$ carbide is stable only up to $\sim 500^\circ\text{C}$. To explain its stability beyond that temperature well documented in the literature [33,34], it was necessary to construct a metastable diagram, where the formation of all hcp phases (M_2C carbide), fcc- and $L1_2$ phases was suppressed. The results for the equilibrium and metastable property diagram are presented in Figure 3. All results were obtained using the *JmatPro* software with the Fe-alloy thermodynamic database [35].

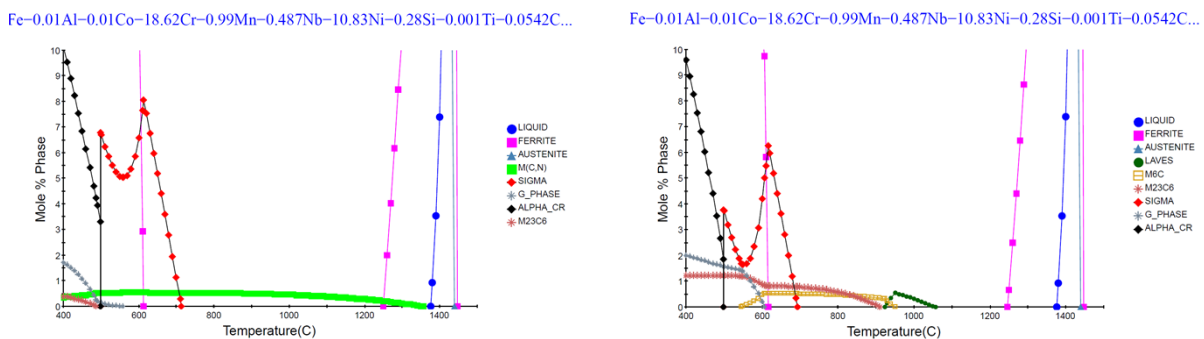


Figure 3. Equilibrium and metastable “phase composition – temperature” diagrams for the 347H alloy composition used in the XMAT program.

All precipitation simulations were done for the 347H alloy composition at 750°C using Thermo-Calc TC-PRISMA software, the TCFE10 and the MOBFE5 thermodynamic and mobility databases (the latest versions). The alloy composition is listed in Table 2 below and is identical to the one used in thermodynamic calculations presented in Figure 3:

Table 2. 347H alloy composition – XMAT Program.

Chemical Element	Fe	Ni	Cr	Mn	Nb	C	Si	Co	Ti	Al	N
Mass. %	68.7188	10.83	18.62	0.99	0.487	0.0542	0.28	0.01	0.001	0.01	0.013

The alloy’s heat treatment procedure included “normalization” for 1 hour at 1,150°C. Therefore, to perform simulations described below, we used the equilibrium calculation at 1,150°C and excluded the primary Nb(C,N) particles from consideration. Similar to Figure 2, we also performed simulations with the full alloy composition (as given in Table 2) and obtained a similar result: while the average primary Nb(C,N) particle size was around 0.3 μm, it did not change appreciably with time up to 1000 hours.

Since the methods of the concurrent precipitation modeling were described in detail earlier. Therefore, we present only the results reproducing the data obtained by Ren et al. [36], Figure 4

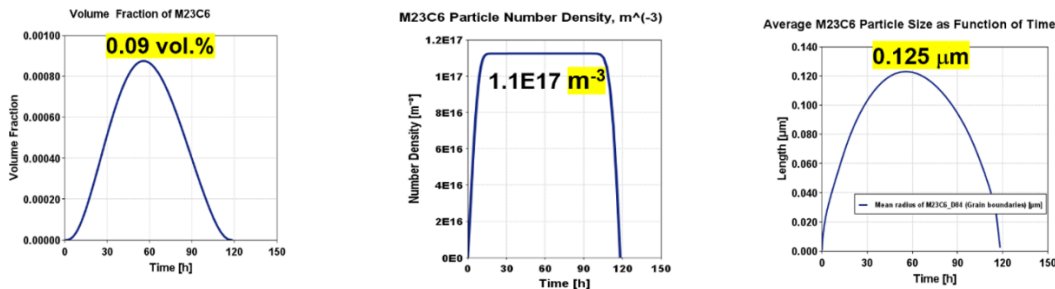


Figure 4. Simulation results for the $M_{23}C_6$ particles and their evolution with time at $T = 750^\circ\text{C}$. **(Left)** Volume fraction of $M_{23}C_6$ as a function of time; **(Center):** $M_{23}C_6$ particle number density; and **(Right)** Average $M_{23}C_6$ particle size as a function of time.

The experimental data by Ren et al. are presented in Table 3; all results correspond to *the maximal values* of volume fraction, number density, and precipitate size [36]

Table 3. Modeling and experimental precipitation data

	Aging time of $M_{23}C_6$ formation	Volume fraction, %	Number density [#]	Size, μm
Simulation	0 through 120h	0.09	$1.1 \times 10^{17} \text{ m}^{-3}$	0.125
Experimental [37]	4h, 24h, and 168h	0.10	$6.0 \times 10^9 \text{ m}^{-2}$	0.480

[#] Experimental results are presented in $\{\text{m}^{-2}\}$, simulation in $\{\text{m}^{-3}\}$. If recalculated to m^{-3} , *experimental* value is $4.7 \times 10^{14} \text{ m}^{-3}$ vs *simulation* value $1.1 \times 10^{17} \text{ m}^{-3}$

Since the experimental study of the secondary Nb(C,N) precipitates encountered difficulties, we report only the results obtained for the metastable $M_{23}C_6$ phase. Its volume fraction attains the highest value of ~ 0.1 vol.% (0.09% in simulation) and decreases to zero after ~ 180 hours (120 hours – our simulations). The number density results are represented qualitatively correctly, if one notices that in all simulations the dimensionality of this property was in $\{m^{-3}\}$, while the experimental results correspond to the in-plane SEM observations and are presented in $\{m^{-2}\}$. Finally, the data on the average particle length is qualitatively correct, but in simulations underestimated by a factor of 4 (~ 480 nm in experiment vs 125 nm in simulations).

In all cases the qualitative representation for all discussed properties was accurate.

1.3 Interaction of dislocations and precipitates during isothermal annealing

In service (during isothermal annealing), the 347H alloy will undergo creep. Complex evolution of the microstructure of phases (precipitates) and defects (vacancies, dislocations, grain boundaries etc.) will take place. TC-PRISMA gives one convenient way to probe these interactions by varying the dislocation density (Advanced Settings, “Dislocation density” parameter). In general, it will depend upon several interdependent and independent factors such as temperature, time, material element geometry, and more. Here, we present our simulation results for isothermal annealing at 700°C by varying dislocation density from $10^{10} m^{-2}$ to $5 \cdot 10^{10} m^{-2}$ (the default value for 347H at 700°C) to $10^{11} m^{-2}$. This is a very conservative estimate because in service conditions and especially for later times, it can vary several orders of magnitude. The results are presented in Figure 5.

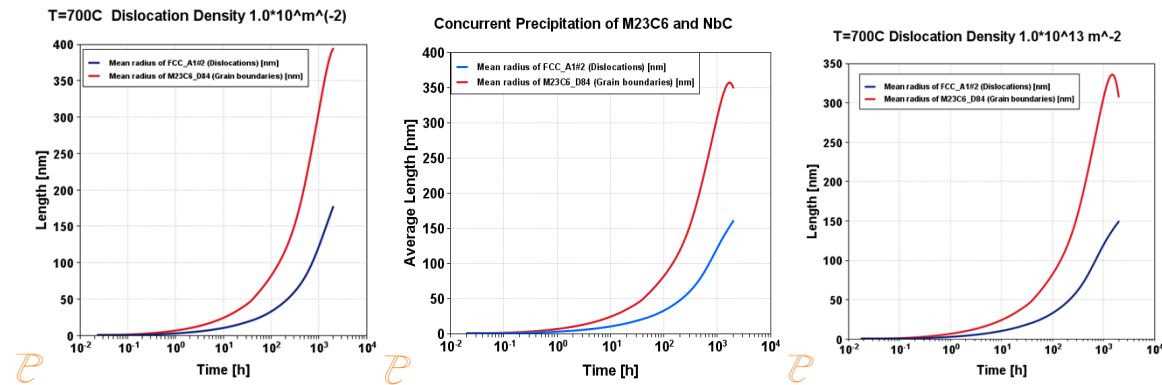


Figure 5 Influence of the dislocation density upon precipitation of secondary NbC and metastable $M_{23}C_6$. Left: Dislocation density $\rho=10^{10} m^{-2}$; Center: $5 \cdot 10^{10} m^{-2}$; Right: $10^{11} m^{-2}$. Note the decrease of the $M_{23}C_6$ precipitate maximal length and the retardation in the Nb(C,N) particle growth with increasing value of ρ .

2. Discussion and Conclusions

The simulation results presented here demonstrated that different sets of precipitation data (at different temperatures, with different heat treatment schedules etc.) could be satisfactorily

described using TC-PRISMA models and simulations. So far, we succeeded in capturing the behavior of the primary and secondary Nb(C,N) particles and the metastable $M_{23}C_6$ precipitates. Further work is necessary to describe a complex process of the concurrent precipitation of primary and secondary Nb(C,N) particles, metastable $M_{23}C_6$ and *the SIGMA phase*. This work is ongoing.

We explored systematically how different precipitation parameters affect the obtained results and concluded that “interfacial energies” of precipitates play a much more important role than anticipated in the beginning. We demonstrate that for Fe-bearing alloys, at least for the 347H, it is necessary to account for the phenomenon of “spin-polarization” of iron atoms. Also, a description of the “nucleation to growth to coarsening” must include three important effects:

(1). For Fe-bearing alloys, the need to account for the spin-polarization of Fe atoms, or a clear demonstration that it can be neglected in calculations.

(2). The role of small and ancillary additions of such elements as nitrogen and boron needs to be better understood. In our preliminary DFT calculations we demonstrated that even the introduction of a single B atom into the fcc-Fe/ $M_{23}C_6$ interface results in a strong ordering effect, appearance of (partially) covalent strong bonding, Figure 5.

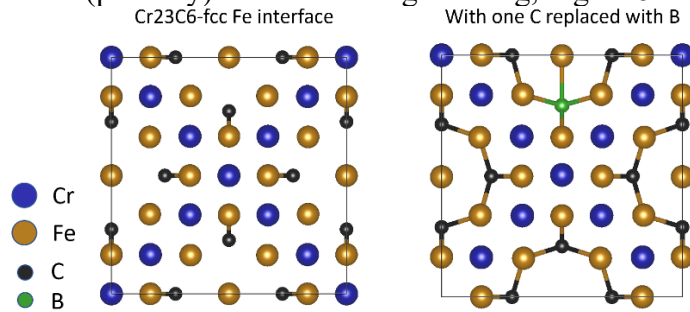


Figure 6. Qualitative illustration of the B-induced ordering effect upon the high-symmetry (001) interface between fcc-Fe and A-terminated $Cr_{23}C_6$ carbide. Note appearance of covalent bonding: Fe atoms prefer to occupy “hollow” positions (not “bridge”) and are projected onto the Cr-C sublattice. The interface was constructed following guidance in [38] for the fcc-Fe/ $M_{23}C_6$ system.

Our preliminary calculations point to the *interfacial energy reduction by $\sim 0.1 J/m^2$* , a very significant value compared to the TC-PRISMA default of $\sim 0.167 J/m^2$. This important result did not depend upon the selection of the ground state for the whole system, which turned out to be a very challenging problem requiring that an additional research effort be made to arrive at the decisive quantification of *the role of several ppm’s of B additions in retarding creep in Fe alloys*.

(3). The loss of coherency and transition to semi-coherent conjugation of a precipitate with its matrix phase. This corresponds to the “elastic contribution” to interfacial energy, in addition to the almost always used “chemical contribution”. Depending upon the lattice misfit parameter it may be negligible or substantial (as in the case discussed here). However, publications with a rigorous description of this transition and the corresponding *increase of interfacial energy describing a less stable semi-coherent state of the system*, are still relatively rare [38,39]. In this work, we use an error function to describe this transition for the metastable $M_{23}C_6$ precipitates.

(4). Transition from coherent to semi-coherent conjugation results in the interfacial energy increase. However, the *subsequent growth* of larger precipitates may result in their different chemical composition (in general, non-uniform, precipitate-size dependent concentration

profiles). In turn, this may result in some variation of the interfacial energy value² and, consequently, the loss of accuracy in predicting the kinetics of precipitation over longer periods of time. In this work, we achieved a satisfactory description of the phenomena accompanying isothermal anneal of the 347H up to 2,200 hours. Obviously, that can't account for the phenomena discussed above and, therefore, extending our results further in time (e.g., several years of service) is hardly feasible in its present form. A revision of the Kampmann-Wagner numerical formalism may fix this problem.

(5). In [31] it was emphasized that the precipitate growth process can be either interfacial energy - controlled, or diffusion – controlled, or both. It is important to have criteria that can [provide guidance on the growth process nature before initiating any computational work. In [31] a significant body of theoretical work was performed for the advanced Kampmann -Wagner Numerical model. It allows to answer many of the questions raised above, but in its numerical implementation, remains very expensive in terms of the needed resources and time.

(6). Finally, all theoretical models and experimental results must be compiled in databases suitable for conducting Data Mining and Machine Learning. These two branches of the AI-assisted physics- and even mathematics-based modeling will help to avoid costly mistakes in the future. This “convergence” of physics + mathematics + data happened in practically all experimental approaches where inverse (ill-posed) problems of the model parametrization are to be solved (e.g., synchrotron XRD, EXAFS and XANES spectroscopy, TEM, SEM, etc.). Even in applied mathematics AI is used for understanding bifurcations (both primary and secondary) from the steady-state branch of solutions and selecting only those modes that contributed decisively to the outcome of the studied nonlinear process [36].

Finally, we want to mention a quantitative demonstration of the interplay of precipitate and dislocation populations, phase and defect microstructures in alloy 347H. At least in principle, this may result in the development of the *chemistry and 2nd phase particle – informed plasticity and creep theory*.

Acknowledgments. We express our sincere gratitude to Ms. Rachel Atencio, the XMAT Program Coordinator. The numerous contributions and technical discussions with our Colleagues from ORNL, LANL, NETL, PNNL, Ames Lab are gratefully acknowledged as well. One of the authors (MVG) expresses his sincere gratitude to the technical personnel of ThermoCalc Software, Inc. – Drs. Paul Mason, Kaisheng (Kevin) Wu, Adam Hope, James Rule, and Conner Sarich (OSU). Without their technical expertise and profound understanding of the problem of precipitation, this work would have been impossible.

² One can speculate that the chemical composition change for a growing precipitate may result in its partial stabilization, i.e., its precipitate/matrix interfacial energy decrease . This will need to be accounted for, especially if simulations are extended to many thousands of hours or days.

Literature

1. J.P. Sanhueza, D. Rojas, O. Prat, J. Garcia, R. Espinoza, C. Montalba, M.F. Melendrez, Precipitation kinetics in a 10.5%Cr heat resistant steel: Experimental results and simulation by TC-PRISMA/DICTRA, *Materials Chemistry and Physics*, 200 (2017) 342-353.
2. Stéphane Gorsse, Yung-Ta Chen, Wei-Che Hsu, Hideyuki Murakami, An-Chou Yeh, Modeling the precipitation processes and the formation of hierarchical microstructures in a single crystal high entropy superalloy, *Scripta Mat.*, 193, (2021) 147-152.
3. Qing Chen, Kaisheng Wu, Gustaf Sterner, Paul Mason, *Journal of Materials Engineering and Performance* **23** (2014) 4193–4196.
4. Anass Assadiki, Vladimir A. Esin, Remi Martinez, Warren J. Poole, Georges Cailletaud, Modeling precipitation hardening in A356+0.5 wt% Cu cast aluminum alloy, *Mat. Sci. Eng. A*, 819 (2021) 141450.
5. Fan Zhang, Lyle E. Levine, Andrew J. Allen, Mark R. Stoudt, Greta Lindwall, Eric A. Lass, Maureen E. Williams, Yaakov Idell, Carelyn E. Campbell, Effect of heat treatment on the microstructural evolution of a nickel-based superalloy additive-manufactured by laser powder bed fusion *Acta Materialia* 152 (2018) 200-214.
6. Pierre Heugue, Daniel Larouche, Francis Breton, Denis Massinon, Rémi Martinez and X.-Grant Chen, Precipitation Kinetics and Evaluation of the Interfacial Mobility of Precipitates in an AlSi7Cu3.5Mg0.15 Cast Alloy with Zr and V Additions, *Metals* 9 (2019) 0777; doi:10.3390/met9070777.
7. Z.-K. Liu, A Materials Research Paradigm Driven by Computation, *JOM*, 2009, **61**(10), p 18–20.
8. L. Kaufman, J. Ågren, CALPHAD, first and second generation—birth of the materials genome. *Scr. Mater.* **70**, 3–6 (2014).
9. G.B. Olson, Computational design of hierarchically structured materials. *Science* **277**, 1237–1242 (1997).
10. M.F. Horstemeyer, *An Introduction to Integrated Computational Materials Engineering (ICME)*, John Wiley & Sons, Inc., New York (2012).
11. Long-Qing Chen, Yuhong Zhao, From classical thermodynamics to phase field method, *Progress in Materials Science*, available online 20 September 2021; [10.1016/j.pmatsci.2021.100868](https://doi.org/10.1016/j.pmatsci.2021.100868).
12. C.E. Campbell, U.R. Kattner, Z.K. Liu, File and data repositories for Next Generation CALPHAD. *Scr. Mater.* **70**, 7–11 (2014).
13. J. Langer, K. Schwartz, Kinetics of nucleation in near-critical fluids, *Physical Review A* 21 (1980).
14. R. Kampmann, R. Wagner, Decomposition of alloys: the early stages, in: Proc. 2nd Acta-Scripta Metall. Conf., Pergamon, Oxford, 1984, pp. 91–103.
15. R. Wagner, R. Kampmann, P. W. Voorhees, Homogeneous second-phase precipitation, *Materials science and technology*, in *Phase Transformations in Materials*, ed. by Gernot Kostorz, p. 948 Wiley-VCH (2001).
16. I.M. Lifshitz, V.V. Slyozov, The kinetics of precipitation from supersaturated solid solutions, *Journal of Physics and Chemistry of Solids*, [Volume 19, Issues 1–2](https://doi.org/10.1016/0022-3697(61)90054-3), April 1961, Pages 35-50; [https://doi.org/10.1016/0022-3697\(61\)90054-3](https://doi.org/10.1016/0022-3697(61)90054-3).

17. D.V. Alexandrov and A.P. Malygin, Nucleation kinetics and crystal growth with fluctuating rates at the intermediate stage of phase transitions, *Model. Sim. Mater. Sci. Eng.* **22** (2014) 015003.
18. Ze Sheng, Manon Bonvalet Rolland, Tao Zhou, Joakim Odqvist, and Peter Hedstrom, Langer–Schwartz–Kampmann–Wagner precipitation simulations: assessment of models and materials design application for Cu precipitation in PH stainless steels, *J Mater Sci* (2021) 56:2650–2671.
19. A. Costa e Silva, L. Nakamura, F. Rizzo, Application Of Computational Modeling to the Kinetics Of Precipitation Of Aluminum Nitride In Steels, *J. Min. Metall. Sect. B-Metall.* **48** (3) B (2012) 471 – 476.
20. A. Costa e Silva, Challenges and opportunities in thermodynamic and kinetic modeling micro-alloyed HSLA steels using computational thermodynamics, *CALPHAD*, **68** (2020) 101720.
21. Bonvalet M, Philippe T, Sauvage X, Blavette D (2015) Modeling of precipitation kinetics in multicomponent systems: application to model superalloys. *Acta Mater* **100** (2015) 169–177.
22. Stechauner G, Kozeschnik E, Thermo-kinetic modeling of Cu precipitation in a-Fe. *Acta Mater* **100** (2015) 135–146.
23. TC-PRISMA v.2021b, ThermoCalc Software Inc., accessed 10/01/2021.
24. H.B. Aaron, D. Fainstain, G.R. Kotler, Diffusion-Limited Phase Transformations: A Comparison and Critical Evaluation of the Mathematical Approximations, *J. Appl. Phys.* **41** (1970) 4404; <https://doi.org/10.1063/1.1658474>.
25. J.E. Morral, J.R. Purdy, Particle coarsening in binary and multicomponent alloys, *Scripta Metall. Mater.*, vol. **30**, iss. **7**, 1 April 1994, pp. 905-908; [https://doi.org/10.1016/0956-716X\(94\)90413-8](https://doi.org/10.1016/0956-716X(94)90413-8).
26. Jou, H. J., Voorhees, P., & Olson, G. B. (2004) *Computer simulations for the prediction of microstructure/property variation in aeroturbine disks*, pp. 877-886. Paper presented at Superalloys 2004 - Tenth International Symposium on Superalloys, Champion, PA, USA; https://doi.org/10.7449/2004/superalloys_2004_877_886.
27. Zh. Guo, W. Sha, Quantification of Precipitation Hardening and Evolution of Precipitates, *Met. Mat. Trans, A*, **43**, 6 (2002) 1273.
28. T. Sourmail, (2002). *Simultaneous Precipitation Reactions in Creep-Resistant Austenitic Stainless Steels* (Cambridge University, Doctoral thesis). <https://doi.org/10.17863/CAM.14212>.
29. T. Sourmail, H.K.D.H Bhadeshia, Modelling simultaneous precipitation reactions in austenitic stainless steels, *CALPHAD*, vol. **27**, iss. **2**, June 2003, pp. 169-175.
30. J. Svoboda, F.D. Fischer, P. Fratzl, E. Kozeschnik, Modelling of kinetics in multi-component multi-phase systems with spherical precipitates - I: Theory *Mat. Sci. Eng. A*, **385** (2004) 166.
31. M. Bonvalet-Rolland, T. Philippe, J. Agren, Kinetic theory of nucleation in multicomponent systems: An application of the thermodynamic extremum principle, *Acta Mat.* **171** (2019) 1-7.
32. A. Borgenstam, L. Höglund, J. Ågren, and A. Engström, DICTRA, a Tool for Simulation of Diffusional Transformations in Alloys, *J. Phase Equilib.*, 2000, **21**(3), p 269–280.

33. Jianguo Yu, Michael V. Glazoff, Michael C. Gao, Ab initio study of energetics and atomic structures of heterophase interfaces of FCC Fe/NbC with and without N doping: from Coherent to Semi-Coherent Interfaces, submitted to JOM (September 2021).
34. Ying-hui Zhou, Chen-xi Liu, Yong-chang Liu, Qian-ying Guo, and Hui-jun Li, Coarsening behavior of MX carbonitrides in type 347H heat-resistant austenitic steel during thermal aging, *Int. J. of Minerals, Metallurgy and Materials*, 23 (2017) 283.
35. Yinghui Zhou, Yanmo Li, Yongchang Liu, Qianying Guo, Chenxi Liu, Liming Yu, Chong Li, and Huijun Li, Precipitation behavior of type 347H heat-resistant austenitic steel during long term high temperature aging, *J. Mater. Res.*, 30 (12 November 2015) pp. 3642-3652.
36. *JmatPro*: <https://www.sentsoftware.co.uk/jmatpro>, accessed 10/01/2021.
37. Q.Q. Ren, Yu. Yamamoto, M.P. Brady, J. Poplawsky, unpublished results, personal communication (15 September, 2021).
38. Elric Barbé, Chu-Chun Fu, and Maxime Sauzay, Fracture of coherent interfaces between an fcc metal matrix and the Cr₂₃C₆ carbide precipitate from first principles, *Phys. Rev. Matls* 2 023605 (2018).
39. Song Lu, John Ågren, Levente Vitos, Ab initio study of energetics and structures of heterophase interfaces: From coherent to semicoherent interfaces, *Acta Mat.*, 156 (2018) 20-30, DOI: [10.1016/j.actamat.2018.06.030](https://doi.org/10.1016/j.actamat.2018.06.030).
40. J.-Y. Lee M.P.J. Punkkinen S. Schönecker Z. Nabi K. Kádas, . Zólyomi, Y.M. Koo, Q.-M. Hu, R. Ahuja, B. Johansson, J. Kollár, L. Vitos, S.K. Kwon, The surface energy and stress of metals, *Surface Science*, 674 (2018) 51-68.
41. D. Wilson, J. Moehlis, Isostable reduction with applications to time-dependent partial differential equations. *Physical Review E*, 94 (2016) 012211. <https://doi.org/10.1103/PhysRevE.94.012211>.